




Corner states in second-order two-dimensional topological photonic crystals with reversed materials

Meng-Cheng Jin , Yong-Feng Gao *, Hao-Zhe Lin, Yi-Han He, and Ming-Yang Chen
School of Mechanical Engineering, Jiangsu University, Zhenjiang 212013, Jiangsu, China

 (Received 9 September 2021; revised 4 April 2022; accepted 28 June 2022; published 14 July 2022)

Recently, topological corner states have been extensively investigated in second-order topological photonic crystals (STPCs). However, most square lattice STPCs are proposed based on the two-dimensional (2D) Su-Schrieffer-Heeger (SSH) model. In this work, we propose a photonic crystal (PC) that goes beyond the 2D SSH model. The unit cell (UC) of the PC is only composed of a dielectric cylinder in an air background (or an air hole in a dielectric slab). The topological trivial or nontrivial photonic band gap of the cylinder-in-air or hole-in-slab UC can be confirmed from the value of 2D polarization. Remarkably, photonic band gaps form directly without any intermediate transition. 2D bulk states, one-dimensional edge states, and zero-dimensional corner states are generated hierarchically in the box-type combination structures composed of trivial and nontrivial PCs. By comparing the perfect and defective structures, the corner states show strong robustness against the defects. The proposed configurations provide a simpler platform for exploring topological corner states in photonic systems, which have great potential for application in integrated nanophotonic devices.

DOI: [10.1103/PhysRevA.106.013510](https://doi.org/10.1103/PhysRevA.106.013510)

I. INTRODUCTION

Photonic crystals (PCs), as an excellent platform for manipulating light transmission, are periodic optical materials that impact the motion of photons in a similar way as ionic lattices in solids affecting electrons motion [1]. The dielectric cylinders of PCs can be manufactured with different materials to form some desired configurations in terms of shapes and layouts. Therefore, many topological phases, including quantum Hall phase [2,3], quantum spin Hall phase [4–7], and the quantum valley Hall phase [8–10], can be realized in the optical frequency based on the platform of PCs. Topological edge states have been demonstrated in PCs fabricated by gyromagnetic materials or all-dielectric materials, which can propagate along the topological interface unidirectionally with the immunity of backscattering [11–16]. Beyond the bulk-boundary correspondence principle, higher-order topological insulators (HOTIs) have been proposed in two-dimensional (2D) quantized quadrupole insulators [17]. Generally, an m th-order topological insulator (TI) in n dimensions has topological edge states at the $(n-m)$ -dimensional boundaries [17–21]. For example, a second-order TI in two-dimensional (2D) systems has both one-dimensional edge states and zero-dimensional corner states [21–25]. Second-order 2D TIs have been proposed both theoretically and experimentally in various systems, such as mechanical resonators, waveguide arrays, microwave circuits, phononic crystals, and photonic crystals [19–44]. Second-order topological photonic crystals (STPCs) have been extensively studied in square lattice [21–25], kagome lattice [31], and hexagonal lattice [19,27].

Hitherto, STPCs with square lattice are mainly proposed on the basis of the 2D Su-Schrieffer-Heeger (SSH) model [21–25], unit cells (UCs) of square lattice are mainly composed of four identical cylinders in an air background or four identical air holes in a slab [21–25,33], and the topological transition is realized based on shrunken and expanded operations on UCs. Here, as an exploration, we aim to investigate STPCs beyond the 2D SSH model.

In this paper, we propose a square lattice PC with reversed materials; the UCs of these PCs are only composed of a dielectric cylinder in an air background and an air hole in a dielectric slab, respectively, which can be seen as an extension of the photonic 2D SSH model. Nevertheless, the cylinder-in-air PC exhibits trivial topology; the hole-in-slab PC has nontrivial topology. Trivial and nontrivial photonic band gaps (PBGs) can be formed directly in two PCs without any intermediate transition. 2D bulk states, one-dimensional edge states, and zero-dimensional corner states are generated hierarchically in a box-type combination structure composed of trivial and nontrivial PCs. The corner states with robustness exist in the gap between bulk states and edge states.

II. NONTRIVIAL TOPOLOGICAL PHASES IN 2D SSH MODEL

The 2D SSH model can be illustrated by a square lattice tight-binding structure as shown in Fig. 1(a) [45], where a UC is composed of four atoms, intracellular hopping w is indicated by the black bond, and intercellular hopping v is denoted as the red bond. The Hamiltonian $H(k)$ is given by

*Corresponding author: absgyf69@163.com

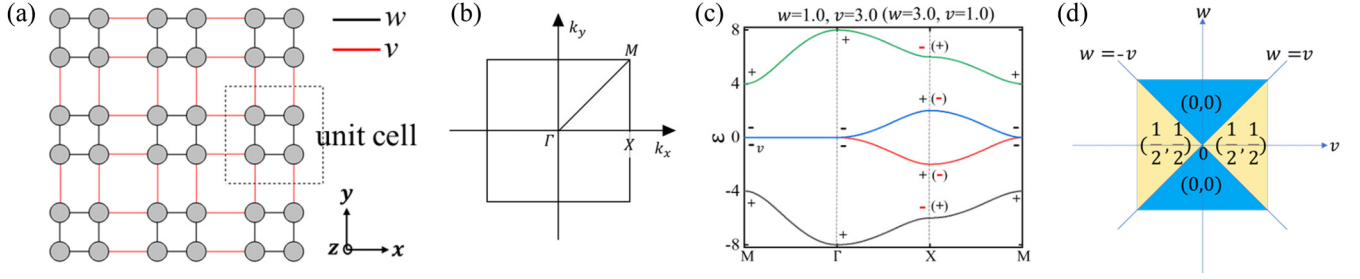


FIG. 1. (a) Schematic of the 2D SSH model. The square lattice UC is composed of four atoms. The intracell hopping and the intercell hopping are represented by w and v , respectively. (b) Corresponding first BZ of the square lattice in (a). (c) Band structures of 2D SSH model with $w = 1.0, v = 3.0$ ($w = 3.0, v = 1.0$). The parities at symmetric points Γ and X are marked by “ \pm ,” respectively. (d) Topological phase diagram for the 2D SSH model in terms of 2D polarization. When $|w| < |v|$, nontrivial phases appear with 2D polarization of $(1/2, 1/2)$.

the following expression [45]:

$$\begin{pmatrix} 0 & w + v \exp(ik_x) & w + v \exp(-ik_y) & 0 \\ w + v \exp(-ik_x) & 0 & 0 & w + v \exp(-ik_y) \\ w + v \exp(ik_y) & 0 & 0 & w + v \exp(ik_x) \\ 0 & w + v \exp(ik_y) & w + v \exp(-ik_x) & 0 \end{pmatrix} = \varepsilon \psi, \quad (1)$$

in which $\psi = (\phi_1, \phi_2, \phi_3, \phi_4)$ represents the bases of the sites of four atoms in the UC, and k_x and k_y are the wave numbers along the x direction and y direction in the first Brillouin zone (BZ), as depicted in Fig. 1(b). Further, band structures can be obtained by solving the Hamiltonian $H(k)$ in the momentum space [44]. Band structures for $(w, v) = (1.0, 3.0)$ and $(w, v) = (3.0, 1.0)$ are displayed in Fig. 1(c). For systems with spatial inversion symmetry, we can calculate the matrix elements of the parity operator in the 2D SSH model, $\langle \psi_i | P | \psi_i \rangle = \pm 1$, where P is the parity operator. Parities at high symmetric points Γ and X are denoted by the sign of “ \pm ” [46]. Parities of the first band at the X point transform its sign between the models with $(w, v) = (1.0, 3.0)$ and $(w, v) = (3.0, 1.0)$, which demonstrates a topological phase transition between the two models [45]. The 2D polarization can be used to describe the topology for the 2D SSH model, which can be expressed as [45]

$$\vec{P} = \frac{1}{2\pi} \int dk_x dk_y \text{Tr}[\vec{A}_m(k_x, k_y)], \quad (2)$$

where $\vec{A}_m(k_x, k_y) = i \langle \psi_m(\vec{k}) | \partial_k | \psi_m(\vec{k}) \rangle$; here $|\psi_m(\vec{k})\rangle$ represents the periodic Bloch function of the m th band, and \vec{k} denotes the wave vector. Inversion symmetry reveals that the value of \vec{P} is determined by the parities at Γ and X (Y) points [45]:

$$P_i = \frac{1}{2} \left(\sum_n q_i^n \text{modulo } 2 \right), \quad i = x, y, \quad (-1)^{q_i} = \frac{\eta(X_i)}{\eta(\Gamma)}, \quad (3)$$

where η represents the parity of the band at the high symmetric point and the summation $\sum_n q_i^n$ is for all the occupied bands. Here, on account of C_4 symmetry, P_x is equal to P_y , namely, $P_x = P_y$. For the model with $(w, v) = (1.0, 3.0)$, $P = (P_x, P_y) = (1/2, 1/2)$ can be obtained. This model is in a nontrivial topology. Analogously, when $(w, v) = (3.0, 1.0)$,

$P = (P_x, P_y) = (0, 0)$ can be obtained. This indicates that the model has a trivial topology. Based on the value of 2D polarization, we found that the critical point of topological phase transition is $|w| = |v|$. Further, the topological phase diagram of the 2D SSH model is plotted in Fig. 1(d); the model exhibits a topological nontrivial phase for $|w| < |v|$, and the topological trivial phase for $|w| > |v|$.

III. EXTENDED PHOTONIC 2D SSH MODEL BASED ON PCs WITH REVERSED MATERIALS

PCs, regarded as artificial atoms, can be used to modulate electromagnetic waves and possess photonic band structures. Medium columns with finite height along the z direction are periodically distributed in the x and y directions for three dimensional (3D) PCs, and the field distribution is uniform along the z direction of 3D PCs. To simplify the model, we set the medium columns with infinite height along the z direction. Therefore, a 3D model has degenerated into a 2D model [27]. Here, 2D square lattice PCs beyond the 2D SSH model are shown in Figs. 2(a) and 2(d). Figure 2(a) depicts a cylinder-in-air UC composed of a dielectric cylinder in an air background, and Fig. 2(d) shows a hole-in-slab UC comprised of an air hole in a dielectric slab. As shown in Figs. 2(a) and 2(d), two UCs can be divided into four parts respectively, obeying C_{4v} point group symmetry.

The lattice constant a is set to 519 nm as the base parameter. The blue region indicates the dielectric material silicon with $\varepsilon_r = 12$, while the other region is the air background with $\varepsilon_0 = 1$. R_1 and R_2 denote the radii of the dielectric cylinder and the air hole respectively. Herein, we only consider the transverse-magnetic (TM) mode of proposed PCs, and transverse-electric mode can be investigated analogously. The numerical simulations are performed by using COMSOL MULTIPHYSICS (a commercial finite-element software). The Floquet periodic boundary condition enables analysis of a

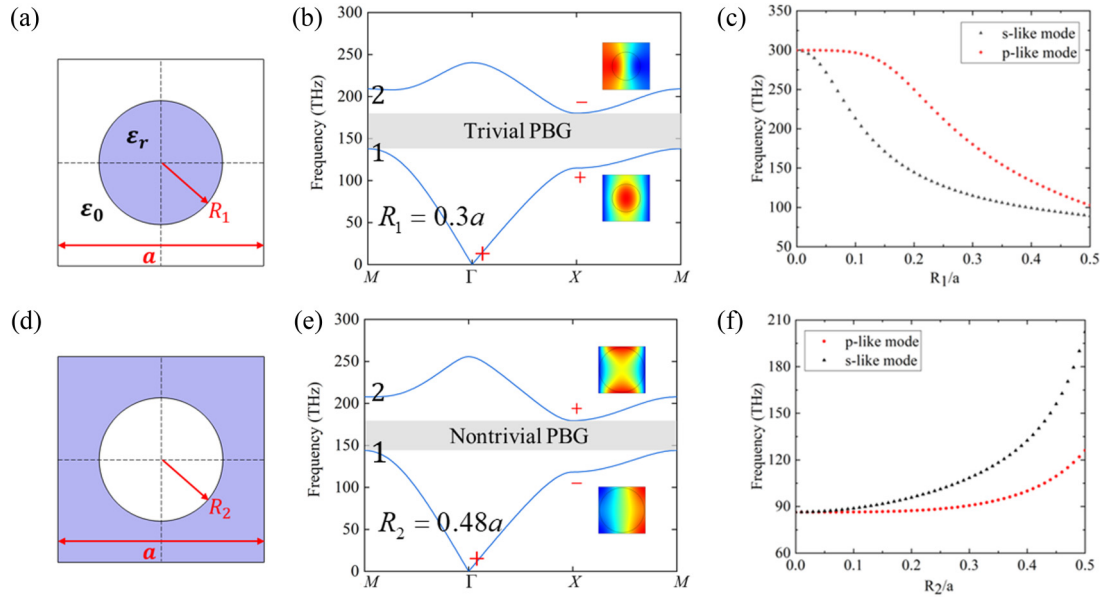


FIG. 2. (a) UC of cylinder-in-air PC; the blue and white regions represent dielectric cylinders with $\epsilon_r = 12$ and air background with $\epsilon_0 = 1$, respectively. The lattice constant and the radius of the cylinder are denoted as a and R_1 . (b) Band structures of the cylinder-in-air PC with $R_1 = 0.3a$. The insets are E_z field distributions of the eigenstates and parities at X point. (c) Frequencies of the first two bands at X point with respect to R_1/a . The parity of the blue curve is even, the parity of the red curve is odd, and there is a trivial band gap between the two bands. (d) UC of hole-in-slab PC; air holes ($\epsilon_0 = 1$) are embedded in the dielectric slab ($\epsilon_r = 12$). The radius of the air hole is represented as R_2 . (e) Band structures of the hole-in-slab PC with $R_2 = 0.48a$. (f) Frequencies of the first two bands at X point with respect to R_2/a , and there is a nontrivial band gap between the two bands.

structure with periodicity, which can increase the calculation efficiency [47]. Therefore, we set the Floquet periodic boundary condition as the boundary condition of the UC along the x direction and y direction, which can simulate the periodic arrangement of the UC. Figures 2(b) and 2(e) depict the band structures of two PCs with $R_1 = 0.3a$ and $R_2 = 0.48a$, respectively. There is a band gap between the first and second bands, and the topology of the proposed PC system can be characterized by the 2D polarization P . For a bosonic PC system, the summation $\sum_n q_i^n$ in Eq. (3) runs all the bands below the band gap [48]. Due to the C_{4v} point group symmetry of UCs, $P_x = P_y$ can be obtained. It is noteworthy that there is only one band below the first band gap. Thus, the 2D polarization for the first band gap can be simplified to

$$P_x = P_y = \frac{1}{2}(q_1 \text{ modulo } 2), \quad (-1)^{q_1} = \frac{\eta_1(X)}{\eta_1(\Gamma)}, \quad (4)$$

where η_1 represents the parity of the high symmetric points for the first band, which could be determined by the parities of the E_z field distributions of the eigenstates at the high symmetric points [36,43,44,49]. Here, E_z field distributions of eigenstates at high symmetric point X are illustrated in the insets of Figs. 2(b) and 2(e). For a cylinder-in-air PC with $R_1 = 0.3a$, the frequency of an s -like mode is lower than that of a p -like mode. However, a cylinder-in-air PC with $R_2 = 0.48a$ exhibits a band inversion, i.e., a p -like mode resides in its first band. The parity of the eigenmode profile is determined by the inversion operation relative to the center of the UC. Therefore, the s -like mode has an even parity marked by “+,” whereas the p -like mode has an odd parity marked by “-.” At the high-

symmetry X and Γ points, the parities are presented in the insets of Figs. 2(b) and 2(e) respectively, and there is a parity inversion at the X point between two UCs. Thus, this model has the same parity inversion as the 2D SSH model. Then, by substituting the results of parity distributions into Eq. (4), the 2D polarization with $P = (0, 0)$ can be determined for the band gap in Fig. 2(b), and $P = (1/2, 1/2)$ for that in Fig. 2(e). Therefore, for UC1 with $R_1 = 0.3a$, a topologically nontrivial band gap from 137.99 to 180.14 THz can be obtained, while UC2 with $R_2 = 0.48a$ possesses a topologically trivial band gap ranging from 144.02 to 179.47 THz.

For the 2D SSH in previous studies, trivial and nontrivial UCs possess analogous band structures and there is a critical point between trivial and nontrivial topological phases [21]. However, our proposed extended photonic 2D SSH model does not have a critical point of topological phase transition. Figures 2(c) and 2(f) denote the frequencies of the first two bands at the X point for a cylinder-in-air UC and a hole-in-slab UC, respectively. The parity of the s -like mode is even, and that of the p -like mode is odd. In detail, band degeneracy on the M - X line of the first BZ can be observed in gapless band structure with $R_1 = 0$. Band degeneracy vanishes, and a trivial photonic PBG is opened with $0 < R_1/a \leq 0.5$. Likewise, for hole-in-slab PC, band degeneracy appears at $R_2 = 0$, and the nontrivial PBG never closes with $0 < R_2/a \leq 0.5$. Explicitly, $P = (0, 0)$ for a cylinder-in-air UC ($0 < R_1/a \leq 0.5$) and $P = (1/2, 1/2)$ for a hole-in-slab UC ($0 < R_2/a \leq 0.5$) can be obtained, which means that cylinder-in-air and hole-in-slab UCs possess trivial and nontrivial band gaps respectively. For cylinder-in-air and hole-in-slab PCs, their PBGs do not have the process of intermediate transition.

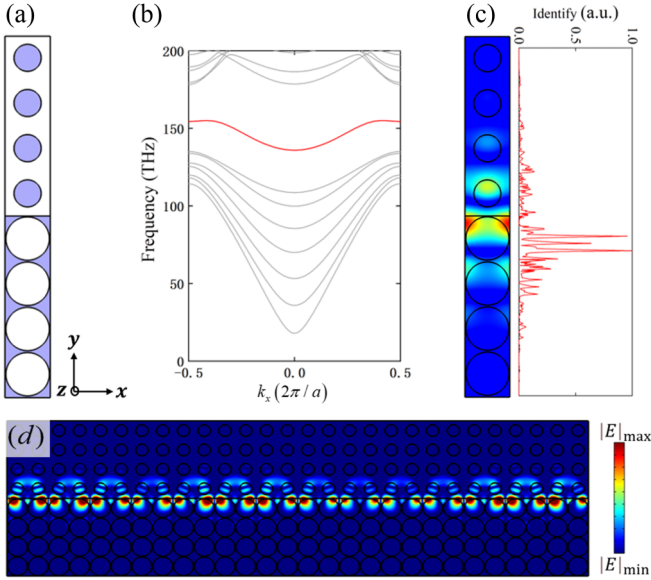


FIG. 3. (a) A supercell composed of topologically trivial PC (cylinder-in-air PC with $R_1 = 0.3a$) and nontrivial PC (hole-in-slab PC with $R_2 = 0.48a$). (b) Dispersion relation of the configuration; the gray curves denote the band of bulk states and the red curve represents the edge states. (c) Simulated electric field distribution of the edge state at 154.48 THz ($k_x = 0.2 \times 2\pi/a$). Right panel: the normalized electric field identify along the y direction. (d) Electric field intensity distribution at 143.50 THz along the interface of two regions with different topologies.

IV. TOPOLOGICAL EDGE STATES

To demonstrate edge states existing at the interface between two different topological regions, we only consider the supercell composed of topologically trivial PCs (cylinder-in-air PC with $R_1 = 0.3a$) and nontrivial PCs (hole-in-slab PC with $R_2 = 0.48a$) as shown in Fig. 3(a). For boundaries of combined structure in Fig. 3(a), the upper and lower boundaries are set as perfect electrical conductors to simplify our configuration, and the left and right boundaries are set to satisfy Floquet periodic boundary conditions. Then, we calculate the frequencies of the wave by solving the eigenvalue

problem based on a periodical scan of the wave vector k_x . The simulated band structure of this configuration is shown in Fig. 3(b), where an edge state (marked by the red curve) emerges at the band gap of bulk states (marked by the gray curve). The simulated electric field distribution of this configuration at 154.48 THz is shown in Fig. 3(c), where the electric field distribution is normalized into the range of $[0, 1]$ [41]. The electric field is concentrated at the interface between two different PCs, and decreases sharply along the y direction. Furthermore, the measured electric field distribution of edge state at 143.50 THz is shown in Fig. 3(d), which reveals that the electric field is confined at the interface between different topological regions [22,23].

V. TOPOLOGICAL CORNER STATES

To investigate the zero-dimensional corner states, we construct two box-type combination structures as shown in Fig. 4. As shown in Fig. 4(a), nontrivial UCs are encompassed by trivial UCs. And the structure in Fig. 4(b) is obtained by exchanging the position of trivial and nontrivial PC in Fig. 4(a). The band structures of trivial PCs (cylinder-in-air PC with $R_1 = 0.3a$) and nontrivial PCs (hole-in-slab PC with $R_2 = 0.48a$) are shown in Figs. 2(b) and 2(e), respectively. The boundary condition of the square structure is set as the perfect electric conductor. The numerical calculation of the discrete spectrum of modes for the combined structure [see in Fig. 4(a)] is shown in Fig. 5(a). Figure 5(a) shows a series of eigenstates, such as bulk states, edge states, and corner states. Clearly, edge states and corner states exist in the band gap of bulk states, and four nearly degenerated corner states are marked by C_1, C_2, C_3, C_4 respectively. The frequencies of four corner states are $f_{C_1} = 169.37790$ THz, $f_{C_2} = 169.37831$ THz, $f_{C_3} = 169.37837$ THz, $f_{C_4} = 169.37969$ THz, respectively. Remarkably, four corner states are not completely degenerate, with few differences in frequency. For example, the frequency difference between C_2 and C_3 is only 0.00006 THz. Additionally, a topological index for the corner state can be defined as

$$\mathcal{Q}^c = \frac{1}{4}([X_1] + 2[M_1] + 3[M_2]), \quad (5)$$

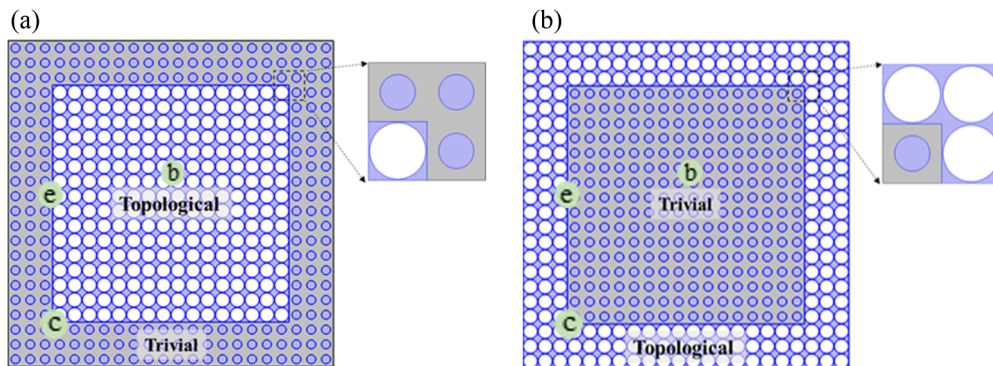


FIG. 4. (a) Box-type combination structure constructed by 16×16 array of topologically nontrivial UCs and three-layer trivial UCs; topological UCs are encompassed by trivial UCs. The bulk probe, edge probe, and corner probe are placed at positions marked by three circles with different letters, respectively. Right panel: enlarged view of the corner. (b) Schematic plot of box-type combination structure; trivial UCs are encompassed by topological UCs.

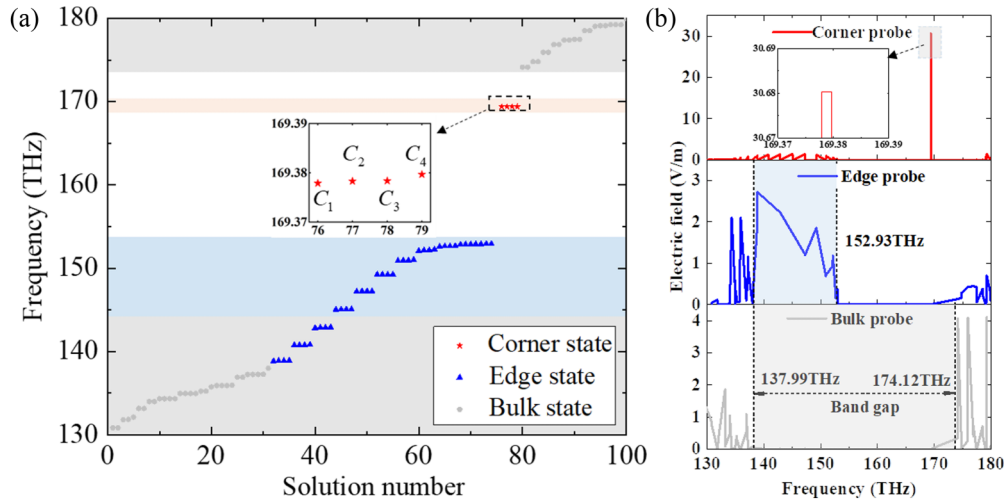


FIG. 5. (a) Numerical calculation of the discrete spectrum of modes for the combined structure in Fig. 4(a). Gray, blue, and red dots denote bulk, edge, and corner states, respectively. Four corner states around 169.38 THz are marked by C_1 , C_2 , C_3 , C_4 , respectively. (b) Electric field spectrum measured by bulk, edge, and corner probes [see in Fig. 4(a)]. Bottom plane: electric field measured by bulk probe; band gap ranges from 137.99 to 174.12 THz. Middle plane: electric field measured by edge probe; edge states range from 137.99 to 152.93 THz. Top plane: electric field measured by corner probe, corner states around 169.38 THz; the inset is the enlarged diagram of electric field around 169.38 THz.

where $[\Pi_p] = \#\Pi_p - \#p$, and $\#\Pi_p$ denotes the number of bands underneath the PBG, in which $\Pi_p = e^{[2\pi i(p-1)]/4}$, where $p = 1, 2, 3, 4$. Π represents high symmetric points (X , M , and Γ) at the first BZ. Herein, the hole-in-slab PC (nontrivial PC) has $[X_1] = -1$, $[M_1] = 1$, and $[M_2] = 0$. Therefore, the corner topological index for the hole-in-slab PC is $Q^c = 1/4$, indicating 1/4 fractionalized eigenstates (corner states) at each of the four corners [23,50].

As shown in Fig. 4(a), three probes are set in the bulk, edge, and corner of the combination structure to measure the electric field, with notations of bulk probe, edge probe, and corner probe, respectively. The measured electric field spectra for those probes are shown in Fig. 5(b). The electric field spectra of the bulk probe are shown at the bottom of Fig. 5(b). There is no electric field from 137.99 to 174.12 THz, which reveals the range of photonic band gap. The electric field spectra of the edge probe are shown in the middle of Fig. 5(b); although the range from 137.99 to 152.93 THz is in the photonic band gap, the edge probe still detects electric field strength. Therefore, the range of edge states is from 137.99 to 152.93 THz. The edge states can propagate along the boundary of trivial and topological regions in the combination structure. In the gap between bulk states and edge states, topological corner states around 169.38 THz can be identified from the top of Fig. 5(b), which has extremely electric field localization compared with the bulk and edge states. The enlarged view of measured electric field for corner probe around 169.38 THz is shown in the inset of the top of Fig. 5(b). We simulate the electric field distributions of bulk states, edge states, and corner states as shown in Fig. 6. The electric field profile of the bulk state at 135.24 THz is presented in Fig. 6(a), revealing that the bulk state can spread in the region of bulk. Figures 6(b)–6(d) exhibit the electric field profiles of three nearly degenerated edge states at 138.89163, 138.89169, and 138.91573 THz, respectively. Obviously, the strength of the field is significantly strong at the boundary of two different topological regions, and extremely weak in the bulk. Additionally, Figs. 6(e)–

6(h) present the electric field profiles of four corner states C_1 , C_2 , C_3 , C_4 , respectively. Corner states are almost totally concentrated at the four corners with strong localization, respectively.

Further, we investigate another type of combined structure as shown in Fig. 4(b). In this case, a 16×16 array of topologically trivial PCs (cylinder-in-air PC with $R_1 = 0.3a$) is surrounded by a three-layer nontrivial PC (hole-in-slab PC with $R_2 = 0.48a$). Therefore, this combined structure has disparate interfaces of two different topologies compared with the structure in Fig. 4(a). According to the discrete spectrum of modes in Fig. 7(a), 2D bulk states, one-dimensional edge states, and zero-dimensional corner states are generated hierarchically, and four topological corner states are marked with by C_1 , C_2 , C_3 , C_4 . C_2 and C_3 are degenerated around 154.65 THz, C_1 with 154.64 THz is lower, C_4 with 154.66 THz is higher. The bulk probe, edge probe, and corner probe are set in the positions of bulk, edge, and corner of the combination structure to measure the electric field intensity, respectively. Figure 7(b) exhibits the measured electric field spectra of those probes. The bulk band gap from 144.02 to 174.64 THz, edge states from 137.99 to 152.93 THz, and corner states around 154.65 THz can be revealed in Fig. 7(b). The inset at the top of Fig. 7(b) exhibits the enlarged view of measured electric field for the corner probe around 154.65 THz. According to the measured electric field for corner and edge probes around 154.65 THz, we find that a weak electric field can be measured at the boundary with the frequency of a corner state, which illustrates that the corner state is not completely localized at the corner. Figure 7(c) exhibits the electric field distributions of four corner states C_1 , C_2 , C_3 , C_4 , respectively. Then, we compare corner states between two combined structures with reversed boundaries. Figures 5 and 6 present the corner states of combined structure with nontrivial UCs embedded into the trivial UCs; four corner states are almost concentrated at the four corners respectively and exhibit strong localization. However, for the reversed boundary,

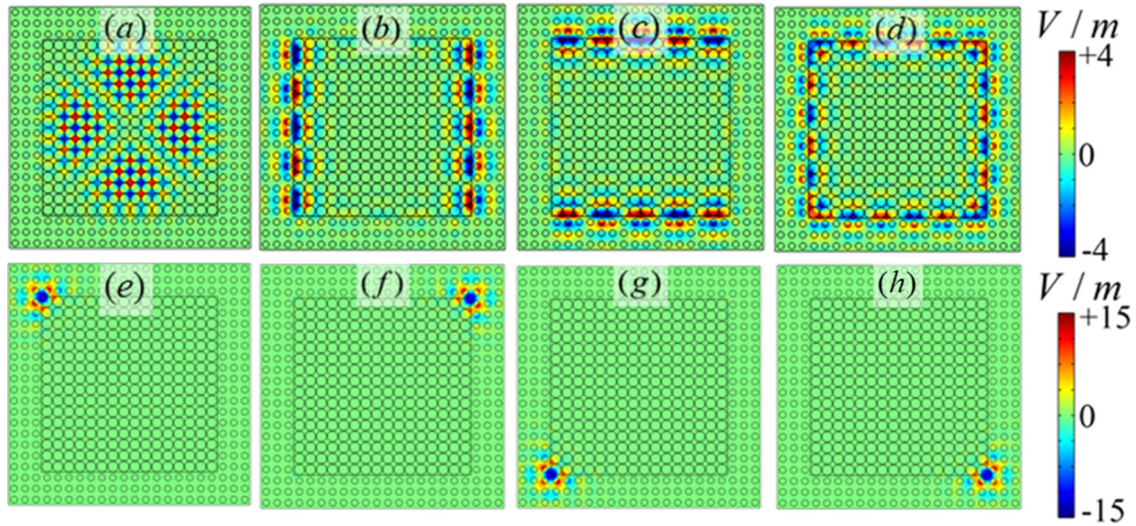


FIG. 6. Simulated electric field distributions of bulk, edge, and corner states, respectively. (a) Bulk state: $f_{\text{bulk}} = 135.24$ THz. (b)–(d) Edge states: $f_{\text{edge}} = 138.89163$ THz, $f_{\text{edge}} = 138.89169$ THz, $f_{\text{edge}} = 138.91573$ THz, respectively. (e)–(h) Corner states: $f = f_{C_1}$, $f = f_{C_2}$, $f = f_{C_3}$, $f = f_{C_4}$, respectively.

i.e., a combined structure with trivial UCs embedded into the nontrivial UCs, four corner states have lower frequency degeneracy and weaker localization.

To study the robustness of the topological corner states against disorders, a composite structure with one corner is designed. The structure in Fig. 8(a) is a perfect structure

without defects. A probe is set at the position of the corner to measure the electric field. The electric field spectrum is shown in Fig. 8(c), and the characteristic spectral line of the corner state at 158.3 THz can be observed. The corresponding electric field profile of the corner state is presented in Fig. 8(b), which is almost totally concentrated at the corner

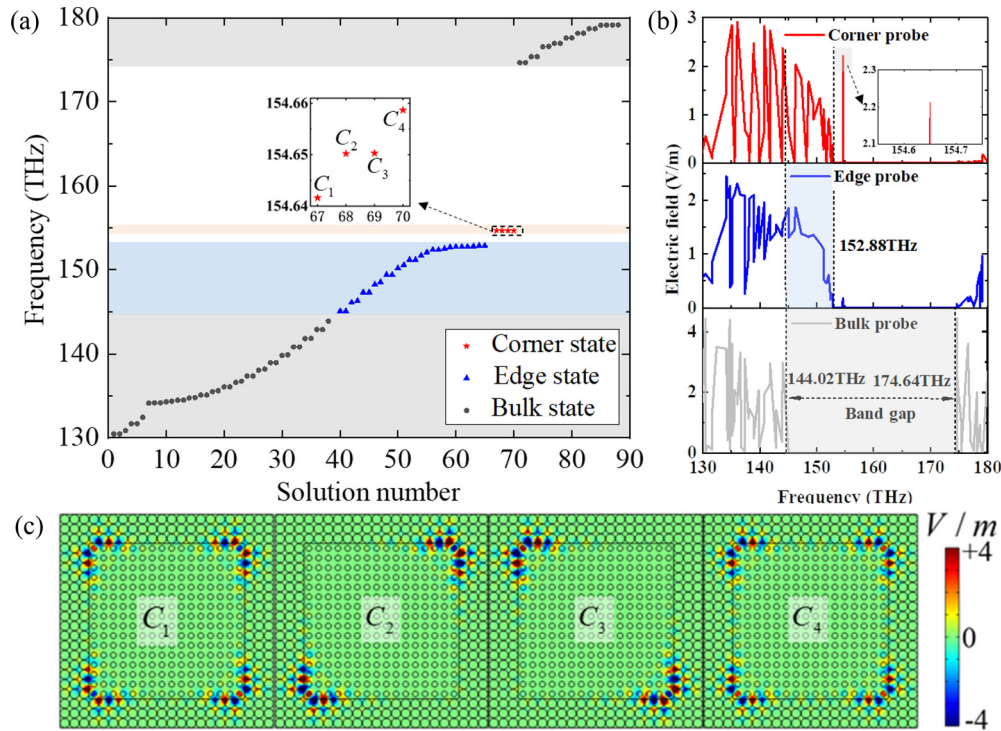


FIG. 7. (a) Numerical calculation of the discrete spectrum of modes for the combined structure in Fig. 4(b). Four corner states around 154.65 THz are marked by C_1 , C_2 , C_3 , C_4 , respectively. (b) Electric field spectrums measured by bulk, edge, and corner probes [see Fig. 4(b)]. Bottom plane: electric field measured by bulk probe; band gap ranges from 144.02 to 174.64 THz. Middle plane: electric field measured by edge probe; edge states range from 144.02 to 152.88 THz. Top plane: electric field measured by edge probe; topological corner states around 154.65 THz. (c) Simulated electric field distributions of four corner states for the box-type combination structure in Fig. 4(b).

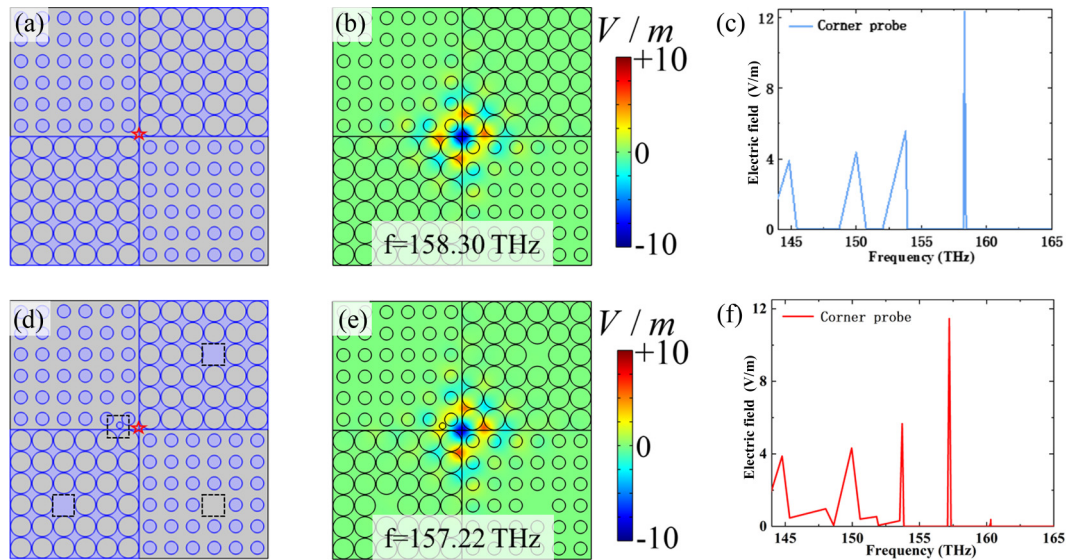


FIG. 8. (a) Box-type combination structure with one corner; the position of probe is marked by the red pentagram. (b) The simulated electric field distributions for (a) at 158.3 THz. (c) Electric field spectrum measured by the corner probe in (b). (d) Box-type combination structure with three cavities and an impurity, which are marked by four dotted boxes. (e) Simulated electric field distribution for (d) at 157.22 THz. (f) Electric field spectrum measured by the corner probe in (d).

with strong localization. Then, we consider a structure with defects as shown in Fig. 8(d). Here, three cavities are introduced by removing the medium column or air hole in UCs, and by inserting an additional medium column for impurity. According to the electric field spectrum in Fig. 8(f), we can confirm that the frequency of corner state is 157.22 THz. The corresponding electric field distribution at 157.22 THz is shown in Fig. 8(e), where the electric field is concentrated at the corner. Despite the introduction of cavities and impurity, the corner state remains almost unchanged except for a slight change in the frequency.

VI. CONCLUSION

In this paper, we propose two 2D PCs with reversed materials beyond the 2D SSH model. The UC of a PC has only one dielectric cylinder in the air background or one air hole in the dielectric slab. Nevertheless, there is no critical point of topological phase transition in our proposed PCs. The cylinder-in-air PC exhibits a trivial topology, while the hole-in-slab PC has a nontrivial topology. Therefore, we can

realize the topological phase transition by exchanging the materials between the cylinder and the background. 2D bulk states, one-dimensional edge states, and zero-dimensional corner states are generated hierarchically in the configuration composed of these two PCs. Four almost degenerated corner states around 169.38 THz arise in the band gap. The corner states are almost fully concentrated at the four corners, respectively. By comparing corner states in perfect and defective structures, it is demonstrated that corner states are robust to defects. The presented results promise wide application prospects of topological edge and corner states for topological photonic devices.

ACKNOWLEDGMENTS

This work was supported by the Project of Zhenjiang Key Laboratory of Advanced Sensing Materials and Devices (Grant No. SS2018001), the Postgraduate Research & Practice Innovation Program of Jiangsu Province (Grant No. KYCX22_3628), the Practice and Innovation Training Project of College Students in Jiangsu University (Grants No. 202110299419X and No. 202110299423X).

- [1] E. Yablonovitch, Inhibited Spontaneous Emission in Solid-State Physics and Electronics, *Phys. Rev. Lett.* **58**, 2059 (1987).
- [2] S. Raghu and F. D. M. Haldane, Analogs of quantum-Hall-effect edge states in photonic crystals, *Phys. Rev. A* **78**, 033834 (2008).
- [3] S. Raghu and F. D. M. Haldane, Possible Realization of Directional Optical Waveguides in Photonic Crystals with Broken Time-Reversal Symmetry, *Phys. Rev. Lett.* **100**, 013904 (2008).
- [4] L. H. Wu and X. Hu, Scheme for Achieving a Topological Photonic Crystal by Using Dielectric Material, *Phys. Rev. Lett.* **114**, 223901 (2015).
- [5] Y. Yang, Y.-F. Xu, T. Xu, H.-X. Wang, J.-H. Jiang, X. Hu, and Z. H. Hang, Visualization of a Unidirectional Electromagnetic Waveguide Using Topological Photonic Crystals Made of Dielectric Materials, *Phys. Rev. Lett.* **120**, 217401 (2018).
- [6] R. Süsstrunk and S. D. Huber, Observation of phononic helical edge states in a mechanical topological insulator, *Science* **349**, 47 (2015).
- [7] R. E. Christiansen, F. Wang, O. Sigmund, and S. Stobbe, Designing photonic topological insulators with quantum-spin-Hall edge states using topology optimization, *Nanophotonics* **8**, 1363 (2019).

- [8] F. Gao, H. Xue, Z. Yang, K. Lai, Y. Yu, X. Lin, Y. Chong, G. Shvets, and B. Zhang, Topologically protected refraction of robust kink states in valley photonic crystals, *Nat. Phys.* **14**, 140 (2018).
- [9] Y. Kang, X. Ni, X. Cheng, A. B. Khanikaev, and A. Z. Genack, Pseudo-spin–valley coupled edge states in a photonic topological insulator, *Nat Commun.* **9**, 3029 (2018).
- [10] X. Xi, K. P. Ye, and R. X. Wu, Topological photonic crystal of large valley chern numbers, *Photonics Res.* **8**, B1 (2020).
- [11] Y.-F. Gao, Z. Jiang, L.-L. Zhang, L. He, and J. Zhao, Unidirectional propagation of coupled edge states in sandwich topological photonic crystals, *J. Appl. Phys.* **124**, 213107 (2018).
- [12] Z. Jiang, Y.-F. Gao, L. He, J.-P. Sun, H. Song, and Q. Wang, Manipulation of pseudo-spin guiding and flat bands for topological edge states, *Phys. Chem. Chem. Phys.* **21**, 11367 (2019).
- [13] Y.-F. Gao, M.-C. Jin, Q. Zhou, Q.-C. Hou, J.-P. Sun, H. Song, and B.-W. Shen, Non-spin-mixing defect modes in the split-ring dielectric photonic crystals, *Opt. Commun.* **492**, 126963 (2021).
- [14] M.-C. Jin, Y.-F. Gao, Q.-L. Ma, W. Zhang, H. Song, and J.-P. Sun, Regularly multiple double dirac cones in photonic bands and topological transitions of all-dielectric photonic crystals, *Phys. Rev. Materials* **5**, 024204 (2021).
- [15] Y.-T. Fang, Z.-X. Wang, E.-P. Fan, X.-X. L, and H.-J. Wang, Topological phase transition based on structure reversal of two-dimensional photonic crystals and construction of topological edge states, *Acta Phys. Sin.* **69**, 184101 (2020).
- [16] L.-N. Chen, L.-J. Jiang, S. Zhang, R. Zhao, Z. -H. Lan, and W. E. I. Sha, Comparative study of hermitian and non-Hermitian topological dielectric photonic crystals, *Phys. Rev. A* **104**, 033501 (2021).
- [17] W. A. Benalcazar, B. A. Bernevig, and T. L. Hughes, Quantized electric multipole insulators, *Science* **357**, 61 (2017).
- [18] F. Schindler, A. M. Cook, M. G. Vergniory, Z. Wang, S. S. P. Parkin, B. A. Bernevig, and T. Neupert, Higher-order topological insulators, *Sci. Adv.* **4**, eaat0346 (2018).
- [19] M. Proctor, P. A. Huidobro, B. Bradlyn, M. B. de Paz, M. G. Vergniory, D. Bercioux, and A. García-Etxarri, Robustness of topological corner modes in photonic crystals, *Phys. Rev. Research* **2**, 042038(R) (2020).
- [20] E. Khalaf, Higher-order topological insulators and superconductors protected by inversion symmetry, *Phys. Rev. B* **97**, 205136 (2018).
- [21] B.-Y. Xie, H.-F. Wang, H.-X. Wang, X.-Y. Zhu, J.-H. Jiang, M.-H. Lu, and Y.-F. Chen, Second-order photonic topological insulator with corner states, *Phys. Rev. B* **98**, 205147 (2018).
- [22] X.-D. Chen, W.-M. Deng, F.-L. Shi, F.-L. Zhao, M. Chen, and J.-W. Dong, Direct Observation of Corner States in Second-Order Topological Photonic Crystal Slabs, *Phys. Rev. Lett.* **122**, 233902 (2019).
- [23] B.-Y. Xie, G.-X. Su, H.-F. Wang, H. Su, X.-P. Shen, P. Zhan, M.-H. Lu, Z.-L. Wang, and Y.-F. Chen, Visualization of Higher-Order Topological Insulating Phases in Two-Dimensional Dielectric Photonic Crystals, *Phys. Rev. Lett.* **122**, 233903 (2019).
- [24] X. Zhang, H.-X. Wang, Z.-K. Lin, Y. Tian, B. Xie, M.-H. Lu, Y.-F. Chen, and J.-H. Jiang, Second-order topology and multi-dimensional topological transitions in sonic crystals, *Nat. Phys.* **15**, 582 (2019).
- [25] A. Shi, B. Yan, R. Ge, J. Xie, Y. Peng, H. Li, W. E. I. Sha, and J. Liu, Coupled cavity-waveguide based on topological corner state and edge state, *Opt. Lett.* **46**, 1089 (2021).
- [26] M. Kim., Z. Jacob, and J. Rho, Recent advances in 2D, 3D and higher-order topological photonics, *Light Sci Appl.* **9**, 130 (2020).
- [27] B. Xie, G. Su, H.-F. Wang, F. Liu, L. Hu, S.-Y. Yu, P. Zhan, M.-H. Lu, Z. Wang, and Y.-F. Chen, Higher-order quantum spin hall effect in a photonic crystal, *Nat Commun.* **11**, 3768 (2020).
- [28] Y. Ota, F. Liu, R. Katsumi, K. Watanabe, K. Wakabayashi, Y. Arakawa, and S. Iwamoto, Photonic crystal nanocavity based on a topological corner state, *Optica* **6**, 786 (2019).
- [29] M. R. López, Z.-W. Zhang, D. Torrent, and J. Christensen, Multiple scattering theory of non-Hermitian sonic second-order topological insulators, *Commun. Phys.* **2**, 132 (2019).
- [30] Z.-W. Zhang, H.-Y. Long, C. Liu, C. Shao, Y. Cheng, X.-J. Liu, and J. Christensen, Deep-Subwavelength holey acoustic second-order topological insulators, *Adv. Mater.* **31**, 1904682 (2019).
- [31] M. Li, D. Zhirihin, M. Gorbach *et al.*, Higher-order topological states in photonic kagome crystals with long-range interactions, *Nat. Photonics* **14**, 89 (2020).
- [32] L. He, Z. Addison, E. J. Mele, and B. Zhen, Quadrupole topological photonic crystals, *Nat Commun.* **11**, 3119 (2020).
- [33] C. Han, M. Kang, and H. Jeon, Lasing at multidimensional topological states in a two-dimensional photonic crystal structure, *ACS Photonics* **7**, 2027 (2020).
- [34] X. Xie, W.-X. Zhang, X.-W. He, S.-Y. Wu, J.-C. Dang, K. Peng, F.-L. Song, L.-L. Yang, H.-Q. Ni, Z.-C. Niu, C. Wang, K.-J. Jin, X.-D. Zhang, and X.-L. Xu, Cavity quantum electrodynamics with second-order topological corner state, *Laser Photonics Rev.* **14**, 1900425 (2020).
- [35] X.-J. Zhang, B.-Y. Xie, H.-F. Wang, X. Xu, Y. Tian, J.-H. Jiang, M.-H. Lu, and Y.-F. Chen, Dimensional hierarchy of higher-order topology in three-dimensional sonic crystals, *Nat Commun.* **10**, 5331 (2019).
- [36] Y.-F. Chen, F. Meng, Z.-H. Lan, B.-H. Jia, and X.-D. Huang, Dual-Polarization Second-Order Photonic Topological Insulators, *Phys. Rev. Appl.* **15**, 034053 (2021).
- [37] X.-X. Zhou, Z.-K. Lin, W.-X. Lu, Y. Lai, B. Hou, and J.-H. Jiang, Twisted quadrupole topological photonic crystals, *Laser Photonics Rev.* **14**, 2000010 (2020).
- [38] T. Mizoguchi, M. Maruyama, S. Okada, and Y. Hatsugai, Flat bands and higher-order topology in polymerized triptycene: Tight-binding analysis on decorated star lattices, *Phys. Rev. Materials* **3**, 114201 (2019).
- [39] X. Zhang, L. Liu, M.-H. Lu, and Y.-F. Chen, Valley-Selective Topological Corner States in Sonic Crystals, *Phys. Rev. Lett.* **126**, 156401 (2021).
- [40] M. Jung, R. G. Gladstone, and G. Shvets, Nanopolaritonic second-order topological insulator based on graphene plasmons, *Adv. Photonics* **2**, 046003 (2020).
- [41] L. Zhang, Y.-H. Yang, Z.-K. Lin, P.-F. Qin, Q.-L. Chen, F. Gao, E. Li, J.-H. Jiang, B. Zhang, and H.-S. Chen, Higher-Order topological states in surface-wave photonic crystals, *Adv. Sci.* **7**, 1902724 (2020).
- [42] A. E. Hassan, F. K. Kunst, A. Moritz, G. Andler, E. J. Bergholtz, and M. Bourennane, Corner states of light in photonic waveguides, *Nat. Photonics* **13**, 697 (2019).

- [43] Y. Chen, Z. Lan, and J. Zhu, Second-order topological phases in c_4v -symmetric photonic crystals beyond the two-dimensional su-schrieffer–heeger model, *Nanophotonics* **11**, 1345 (2022).
- [44] Y. Chen, Z. Lan, J. Li, and J. Zhu, Topologically protected second harmonic generation via doubly resonant high-order photonic modes, *Phys. Rev. B* **104**, 155421 (2021).
- [45] F. Liu and K. Wakabayashi, Novel Topological Phase with a Zero Berry Curvature, *Phys. Rev. Lett.* **118**, 076803 (2017).
- [46] W. Feng, J. Wen, J. Zhou, D. Xiao, and Y. Yao, First-principles calculation of Z₂ topological invariants within the FP-LAPW formalism, *Comput. Phys. Commun.* **183**, 1849 (2012).
- [47] C. Hakoda, J. Rose, P. Shokouhi, and C. Lissenden, Using Floquet periodicity to easily calculate dispersion curves and wave structures of homogeneous waveguides, in *44th Annual Review of Progress in Quantitative Nondestructive Evaluation*, Vol. 37, AIP Conf. Proc. No. 1949, edited by D. E. Chimenti and L. J. Bond (AIP, Melville, NY, 2018), p. 020016.
- [48] M. Blanco de Paz, M. A. J. Herrera, P. Arroyo Huidobro, H. Alaeian, M. G. Vergniory, B. Bradlyn, G. Giedke, A. García-Etxarri, and D. Bercioux, Energy density as a probe of band representations in photonic crystals, *J. Phys.: Condens. Matter* **34**, 314002 (2022).
- [49] Z. Zhang, M. R. López, Y. Cheng, X. Liu, and J. Christensen, Non-Hermitian Sonic Second-Order Topological Insulator, *Phys. Rev. Lett.* **122**, 195501 (2019).
- [50] S. Leung, Y. Liu, F.-F. Li, C. Liang, Y. Poo, and J.-H. Jiang, Observation of fractional quantum numbers at photonic topological edges and corners, [arXiv:2203.00206](https://arxiv.org/abs/2203.00206).